Correlated errors in phase-shifting laser Fizeau interferometry

Peter J. de Groot*

Zygo Corporation, Laurel Brook Road, Middlefield, Connecticut 06455, USA

*Corresponding author: peterd@zygo.com

Received 27 February 2014; accepted 17 April 2014;
posted 21 May 2014 (Doc. ID 207371); published 30 June 2014

High-performance data processing algorithms for phase-shifting interferometry accommodate adjustment errors in the phase shift increment as well as harmonic distortions in the interference signal. However, a widely overlooked error source is the combination of these two imperfections. Phase shift tuning errors increase the sensitivity of phase estimation algorithms to second-order and higher harmonics present in Fizeau interference signals. I derive an analytical formula for evaluating these errors more realistically, in part to identify the characteristics of the optimal PSI algorithm. Even for advanced algorithms, it is found that multiple reflections increase the error contribution of detuning by orders of magnitude compared with the two-beam calculation and impose a practical limit of 30% in tuning error for sub-nm metrology in a 4%–4% Fizeau cavity. Consequently, a preferred approach for high precision spherical cavities is to use either wavelength tuning in place of mechanical phase shifting or an iterative solver that accommodates unknown phase shifts as a function of field position.

OCIS codes: (120.3180) Interferometry; (120.5050) Phase measurement; (120.6650) Surface measurements, figure.

http://dx.doi.org/10.1364/AO.53.004334

1. Introduction

Modern phase-shifting interferometry (PSI) algorithms have excellent characteristics in the presence of a scaling error in the nominal phase shift increment, which is commonly referred to as calibration or detuning error [1]. The solid line (A) in Fig. 1 for two-beam interference illustrates typical advertised performance, showing that this source of error is, in principle, negligible—a 20% detuning error results in an imperceptible 0.02 nm RMS cyclic (phase dependent) error in a 3D surface map. A separate analysis of resistance to multiple reflections in a Fizeau cavity with proper phase shift adjustment typically shows excellent suppression of the resulting higher-order harmonics in the interference signal.

The impressive performance of well-designed PSI algorithms provides confidence in applications where the phase shift is imperfect or where the phase shift varies across the field, as is the case with fast Fizeau cavities [2,3]. The reality, however, is quite different: the dashed line (B) in Fig. 1 shows that the combined effect of detuning error and the multiple reflections for even weakly reflecting (4%) surfaces results in an error far greater than expected from the two-beam approximation. Although prior work has recognized this phenomenon [4–6], it remains one of the most frequently overlooked sources of error.

This paper reviews the gap between expected and actual performance of PSI in the presence of phase shift detuning in laser Fizeau interferometers. An analytical expression for measurement errors allows for a more realistic evaluation of algorithm behavior, while clarifying the origin of the significant coupling between detuning and multiple reflections. The paper concludes with some recommendations for

1559-128X/14/194334-09$15.00/0

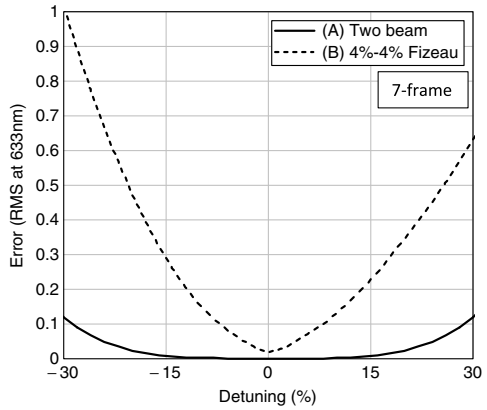

Fig. 1. Sensitivity of a high-performance seven-frame PSI algorithm [7] to phase-shift calibration errors, assuming (A) two-beam interference, as is the usual approach to error analysis, and (B) interference in a laser Fizeau cavity with modest 4% reference and 4% object reflectivities.

mitigating these errors where required for high-precision applications.

2. Is PSI Possible with a Fizeau Cavity?

Somewhat surprisingly, it was not at all obvious in the earliest days of PSI that phase shifting would work well with Fizeau fringes, which are not purely sinusoidal because of multiple cavity reflections. The first PSI algorithms in the 1970s were developed in the context of Twyman Green interferometers [8–10], while at that time most Fizeau systems were visual or used computerized image analysis to trace the interference fringes. Although researchers readily adapted temporal PSI to laser Fizeau interferometers, the potential for error from nonsinusoidal fringes was unclear.

In 1987, Hariharan looked into the problem and found that a then popular three-frame algorithm with a shift of $\pi/2$ between intensity samples had an unacceptable peak-valley phase error of 12° in a Fizeau cavity with 5% reflectivities for both surfaces [11]. Fortunately, he also found that a four-frame algorithm had a much more promising error of 0.6°, which is 20× lower. Hariharan noted that the improvement was the result of Fourier filtering to eliminate the second harmonic or double-pass signal in the Fizeau cavity. In 1989, Bönsch and Bohme rederived the four-frame algorithm and announced that "…the results…show that phase determination by the method of phase shifting interferometry, which was so far restricted to two-beam interferences, can be extended to Fizeau interferences" [12]. Ai and Wyant confirmed the phase error for the four-frame algorithm in 1993 and arrived at the same conclusion as Hariharan: that the four-frame algorithm suppresses the second-harmonic signal in the Fizeau cavity. Dorrío *et al.* repeated the calculation in 1996 for both the three- and four-frame algorithms, using a more general method extendable to other algorithms [13].

Today the most common optical testing interferometer is a laser Fizeau using temporal phase shifting. Researchers and manufacturers have developed algorithms involving more data frames to suppress errors beyond the second harmonic to the third harmonic and even further. These developments improve performance for high-finesse (high reflectivity) cavities, which is an important step forward in flexibility and precision. As an example, the residual error for a 13-frame algorithm derived in 1995 in a 4%–4% cavity is a nearly negligible 0.005° peak-valley error contribution from multiple reflections [14]. A 12-frame algorithm developed by Surrel has even lower errors [15].

Advances in PSI algorithm design would seem to put to rest any concerns about multiple reflections in a Fizeau, provided that we use a 12- or 13-frame algorithm or comparable analysis method. These algorithms enjoy high performance over a wide detuning range for the phase shift ramp as well as suppression of harmonic terms related to multiple reflections in a Fizeau cavity. In 1996, I contributed a paper that concluded that modern algorithms enabled mechanically phase-shifted PSI methods for fast, high NA spherical Fizeau cavities where detuning errors are unavoidable [3]. However, this conclusion was based on the limit case of low reflectivity Fizeau cavities, using an antireflection coated reference, object, or both.

Hibino *et al.* were among the first to examine the more general case of nonsinusoidal fringes and detuning as well as the effects of nonlinear phase shifts in a Fizeau cavity [4,16]. Their work includes recommendations for changes in PSI algorithms. Zhao and Surrel also proposed algorithm designs with this effect in mind, based on the identification of double roots in Surrel's characteristic polynomials [6,17]. In a further study for the LIGO project in 2000, Creath reports a series of numerical simulations for the behavior of eight known PSI algorithms [5], including linear and two-order phase shifter errors for measurements in a plane parallel Fizeau cavity. Creath notes that in this context algorithms have behaviors that depend upon the coupling of the error sources, specifically nonsinusoidal fringes and detuning errors. Malacara *et al.* note as well in that when there are detuning errors, not only the fundamental frequency but also its harmonics are detuned, and this is an important error source [1,18].

In spite of this prior work, it is still commonplace to analyze the detuning performance of PSI algorithms using only the idealized two-beam interference equation [19,20]. Where the multiple reflections are considered, frequently ignored is the simultaneous effect of detuning on the solution. The potential result is an underestimate of this error source, particularly with high-NA spherical cavities of even modest reflectivity.

3. Fizeau Interferometry

In a laser Fizeau interferometer (Fig. 2), the high-coherence light means that multiple reflections

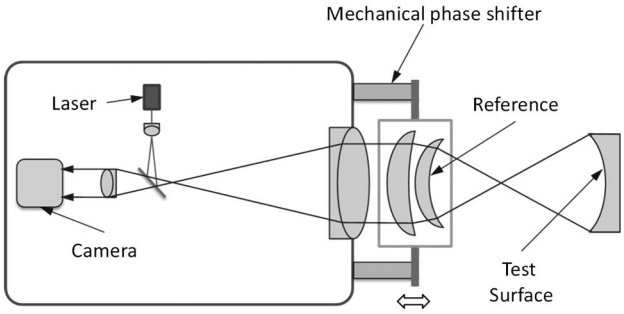

Fig. 2. Laser Fizeau interferometer with a spherical cavity.

between the reference and object surfaces will interfere. The familiar multiple-reflection formula applies for the resulting intensity:

$$I(\theta,t)=\left|\frac{\sqrt{\rho_1}+\sqrt{\rho_2}e^{i[\theta+\alpha(t)]}}{1+\sqrt{\rho_1}\sqrt{\rho_2}e^{i[\theta+\alpha(t)]}}\right|^2, \tag{1}$$

where ρ_1, ρ_2 are the intensity reflectivities of the reference and object surfaces, respectively, and phase changes on reflection have been suppressed as irrelevant to the modeling task at hand. The round-trip phase delay for propagation from one surface to the other is θ, and the time-dependent offset generated by the mechanical phase shifter is $\alpha(t)$. The intensity in Eq. (1) expands as a Fourier series:

$$I(\theta,t)=q+qV_1\cos[\theta+\alpha(t)]+qV_2\cos\{2[\theta+\alpha(t)]\}+qV_3\cos\{3[\theta+\alpha(t)]\}+\ldots, \tag{2}$$

where

$$q=\frac{\rho_1+\rho_2-2\rho_1\rho_2}{1-\rho_1\rho_2}, \tag{3}$$

$$V_1=\frac{1}{q}\frac{2(1-\rho_1)(1-\rho_2)}{1-\rho_1\rho_2}\sqrt{\rho_1\rho_2}, \tag{4}$$

$$V_2=-V_1\sqrt{\rho_1\rho_2}, \tag{5}$$

$$V_3=V_1\rho_1\rho_2, \tag{6}$$

and so on, with the relative contrast V_n of each successive harmonic of order n decreasing in strength by the multiplicative factor $-\sqrt{\rho_1\rho_2}$. These harmonics relate to the interference between wavefronts that differ by the number n of round-trip reflections inside the cavity.

For weak reflections (for example, less than 1%), the progressively weaker harmonics in Eq. (2) may be negligible with respect to the fundamental term of strength V_1. We then have the single-pass or two-beam approximation:

$$I(\theta,t)\approx q+qV\cos[\theta+\alpha(t)], \tag{7}$$

where

$$V\approx\frac{2\sqrt{\rho_1\rho_2}}{q}. \tag{8}$$

The expected interference signal is the solid line (A) shown in Fig. 3.

For high reflectivities, the unique appearance of high-finesse Fizeau interference fringes is evident, as shown by the dashed line (B) in Fig. 3. Here the higher harmonics in Eq. (2) caused by multiple reflections in the cavity generate characteristic asymmetry. Although it is less evident by inspection of the signal shape, the higher harmonics are of course always present, even with low reflectivities for the reference and object surfaces.

An additional complication with a mechanically phase-shifted laser Fizeau when testing spherical optics is the variation of the interference signal frequency with the field position [2,3,10]. The linear mechanical phase shift motion is along the optical axis of the Fizeau cavity, whereas the ray paths are angled, resulting in a cosine error. In the extreme case of a reference surface having a numerical aperture (NA) of 1.0, the edge of the interference pattern does not shift in phase at all.

Figure 4 shows the effect of the spherical geometry on detuning using the adjustment technique recommended by Moore and Slaymaker, which involves reducing the phase shift increment at the vertex so as to balance detuning between the vertex and the edge of the aperture [10]. This graph together with the graph in Fig. 1 enables estimation of the effects of the spherical geometry on cyclic errors in the interferometer. Although the effect is modest for common spherical geometries up to 0.5 NA (equivalent to $f/2$), steeper spheres can become a problem, particularly when taking into account the coexisting issue of multiple reflections.

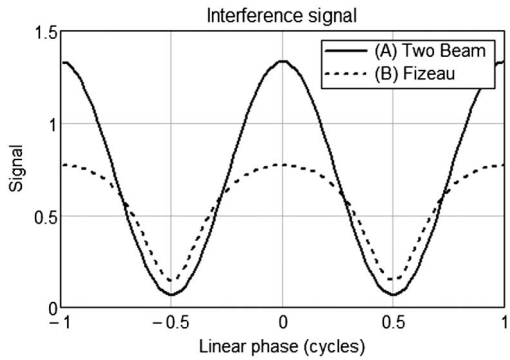

Fig. 3. (A) Interference fringe signal for a linear phase shift in a two-beam interferometer such as a Michelson, Twyman Green, or low-coherence microscope. (B) Interference signal for a laser Fizeau interferometer with reference and object reflectivities, both of which equal 20%.

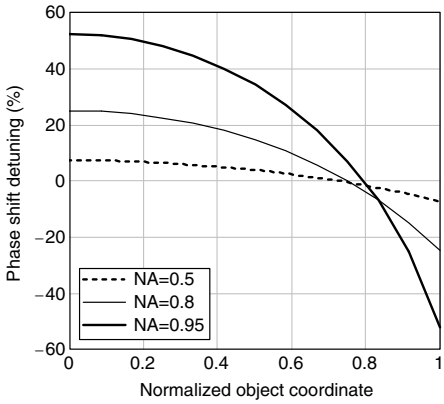

Fig. 4. Phase shift calibration error as a function of the normalized field coordinate in a spherical Fizeau cavity for three different cavity NA values.

4. PSI Algorithm Characteristics

Given that Fizeau fringes include harmonics of the principal interference fringe signal, the path to calculating the effect on PSI of nonsinusoidal Fizeau fringes is to determine the sensitivity of the PSI method to these harmonics. Although PSI harmonic sensitivity is familiar territory [15,21], the approach taken here allows for the detuning and harmonic distortions at the same time. The analysis provides analytical formulae for predicting the magnitude of the correlated error.

In PSI with a linear phase shift centered at zero, the phase shift α_j corresponding to each intensity sample I_j captured by a sequence of camera frames is

$$\alpha_j = \left(j - \frac{P-1}{2}\right)\Delta\alpha, \tag{9}$$

where $\Delta\alpha$ is the phase increment and P is the total number of data samples. As illustrated in Table 1, PSI algorithms have the general form,

$$\tan(\theta) = \frac{\Gamma_c}{\Gamma_s}\frac{R_s(\theta)}{R_c(\theta)}, \tag{10}$$

where

$$R_s(\theta) = \sum_j (h_s)_j I_j \tag{11}$$

$$R_c(\theta) = \sum_j (h_c)_j I_j, \tag{12}$$

where $\Gamma_{s,c}$ constant scaling factors, and h_s, h_c are coefficients sensitive to the modulations $\sin(\alpha_j)$ and $\cos(\alpha_j)$. Typically coefficients h_s, h_c are normalized so that $\Gamma_s = \Gamma_c$, but showing the scaling factors here will prove useful in what follows.

A widely known interpretation of PSI algorithms is to represent the filtering process in the frequency domain, designed to recover the phase of a specific heterodyne frequency generated by phase shifting [21]. An approach to developing filter functions is to first expand the intensity function of Eq. (7) as

$$I_j = qV + qV\cos(\theta)\cos(\alpha_j) - qV\sin(\theta)\sin(\alpha_j), \tag{13}$$

which inserted into Eq. (10) shows that

$$R_s(\theta) = \sin(\theta) q V \Gamma_s, \tag{14}$$

$$R_c(\theta) = \cos(\theta) q V \Gamma_c, \tag{15}$$

where the scaling factors

$$\Gamma_s = -\sum_j (h_s)_j \sin(\alpha_j), \tag{16}$$

$$\Gamma_c = \sum_j (h_c)_j \cos(\alpha_j), \tag{17}$$

quantify the sensitivity to the expected $\sin(\alpha_j)$ and $\cos(\alpha_j)$ modulations.

The idea behind filter functions is to generalize the scaling coefficients $\Gamma_{s,c}$ to evaluate the transfer characteristics of PSI algorithms as a function of signal frequency. Filter functions describe the sensitivity of the numerator and denominator of the right-hand side of Eq. (10) to intensity signals at a frequency ν, which may be different from the design frequency.

Table 1. Representative Fixed-Phase Step PSI Algorithms

Frames	Reference	Step	Algorithm Coefficient Vectors h_s/h_c
3	[22]	$\pi/2$	$\frac{(-1\ \ 0\ \ 1)}{(-1\ \ 2\ \ -1)}$
4	[23]	$\pi/2$	$\frac{(1\ \ 1\ \ -1\ \ -1)}{(-1\ \ 1\ \ 1\ \ -1)}$
7	[7, 24]	$\pi/2$	$\frac{(-1\ \ 0\ \ 7\ \ 0\ \ -7\ \ 0\ \ 1)}{(0\ \ -4\ \ 0\ \ 8\ \ 0\ \ -4\ \ 0)}$
12	[15]	$\pi/3$	$\frac{\sqrt{3}(0\ \ -3\ \ -3\ \ 3\ \ 9\ \ 6\ \ -6\ \ 9\ \ -3\ \ 3\ \ 3\ \ 0)}{(2\ \ 1\ \ -7\ \ -11\ \ -1\ \ 16\ \ 16\ \ -1\ \ -11\ \ -7\ \ 1\ \ 2)}$
15	[3]	$\pi/2$	$\frac{(-0.006\ \ 0\ \ 0.166\ \ 0\ \ -0.870\ \ 0\ \ 1.829\ \ 0\ \ -1.829\ \ 0\ \ 0.870\ \ 0\ \ -0.166\ \ 0\ \ 0.006)}{(0\ \ -0.044\ \ 0\ \ 0.435\ \ 0\ \ -1.392\ \ 0\ \ 2\ \ 0\ \ -1.392\ \ 0\ \ 0.435\ \ 0\ \ -0.044\ \ 0)}$

To simplify the appearance of the math, by definition, a frequency $\nu = 1$ corresponds to the fundamental modulation for a perfectly adjusted system.

For symmetric algorithms, the filter functions have a form similar to Eqs. (16) and (17), but now include a variable fringe frequency ν:

$$F_s(\nu) = -\sum_j (h_s)_j \sin(\nu\alpha_j), \tag{18}$$

$$F_c(\nu) = \sum_j (h_c)_j \cos(\nu\alpha_j). \tag{19}$$

For these equations, I have used the simplifying orthogonality conditions,

$$\sum_j (h_s)_j \cos(\nu\alpha_j) = 0 \tag{20}$$

and

$$\sum_j (h_c)_j \sin(\nu\alpha_j) = 0, \tag{21}$$

for all frequencies—conditions that are satisfied automatically for symmetric algorithms centered about a zero phase shift. It has been shown elsewhere [25] that the filter functions accommodate the effect of frame integration by including a factor $B(\nu)$:

$$F_s(\nu) = -B(\nu)\sum_j (h_s)_j \sin(\nu\alpha_j), \tag{22}$$

$$F_c(\nu) = B(\nu)\sum_j (h_c)_j \cos(\nu\alpha_j). \tag{23}$$

Most commonly,

$$B(\nu) = \frac{\sin(\nu\Delta\alpha/2)}{\nu\Delta\alpha/2}. \tag{24}$$

5. Detuning Errors

As a first example use of filter functions, I rederived a known result for the effect of phase shift detuning error [3]. Recalling from Eq. (10) the basic form of PSI algorithms,

$$\tan(\theta) = \frac{\Gamma_c}{\Gamma_s}\frac{R_s(\theta)}{R_c(\theta)}, \tag{25}$$

a detuning error means that we need to rewrite $R_{s,c}(\theta)$ as

$$R_s(\nu_0, \theta) = \sin(\theta) qV F_s(\nu_0), \tag{26}$$

$$R_c(\nu_0, \theta) = \cos(\theta) qV F_c(\nu_0), \tag{27}$$

where $\nu_0 \neq 1$ is the actual signal frequency as opposed to the design frequency for the algorithm. The corresponding phase error ε_{cal} resulting from detuning is

$$\tan(\theta + \varepsilon_{\text{cal}}) = \frac{F_s(\nu_0)}{F_c(\nu_0)}\frac{\Gamma_c}{\Gamma_s}\tan(\theta). \tag{28}$$

We expand this to

$$\tan(\theta) + [1 + \tan^2(\theta)]\varepsilon_{\text{cal}} = \frac{F_s(\nu_0)}{F_c(\nu_0)}\frac{\Gamma_c}{\Gamma_s}\tan(\theta), \tag{29}$$

which upon solving for ε_{cal} becomes

$$\varepsilon_{\text{cal}}(\nu_0, \theta) = \frac{\tan(\theta)}{1 + \tan^2(\theta)}\left[\frac{F_s(\nu_0)}{F_c(\nu_0)}\frac{\Gamma_c}{\Gamma_s} - 1\right] \tag{30}$$

or

$$\varepsilon_{\text{cal}}(\nu_0, \theta) = [\tau(\nu_0) - 1]\sin(\theta)\cos(\theta), \tag{31}$$

where

$$\tau(\nu_0) = \frac{F_s(\nu_0)}{F_c(\nu_0)}\frac{\Gamma_c}{\Gamma_s}. \tag{32}$$

The standard deviation of the error is

$$\sigma_{\text{cal}}(\nu_0) = \frac{1}{2\sqrt{2}}|\tau(\nu_0) - 1|. \tag{33}$$

These results show that sensitivity to detuning relates primarily to how well the filter functions match for signals that differ from the design frequency. This realization has guided efforts to develop algorithms with reduced sensitivity to detuning [21].

6. Intensity Sensitivity of Detuned PSI Algorithms

The pathway for measurement errors attributable to harmonic distortions is the sensitivity of the algorithm to the additive intensity noise at frequencies other than the fundamental. To calculate the effect of these spurious signals, I define an additive intensity noise n for sample j of amplitude q' at a noise frequency ν' and a phase ξ:

$$n_j(\nu') = q' \cos(\nu'\alpha_j + \xi). \tag{34}$$

The PSI algorithm will pass signals,

$$N_{s,c}(\nu', \xi) = \sum_j (h_{s,c})_j n_j(\nu'), \tag{35}$$

which add directly to the numerator and denominator of Eq. (10). The result is a phase error ε:

$$\tan(\theta + \varepsilon) = \frac{R_s(\theta) + N_s(\nu', \xi)}{R_c(\theta) + N_c(\nu', \xi)}. \tag{36}$$

Expanding Eq. (36) for small phase errors ($\varepsilon \ll 1$),

$$\tan(\theta) + [1 + \tan^2(\theta)]\varepsilon = \tan(\theta)\left[1 + \frac{N_s(\nu', \xi)}{R_s(\theta)} - \frac{N_c(\nu', \xi)}{R_c(\theta)} + \ldots\right], \quad (37)$$

we have to first order

$$\varepsilon(\theta, \xi) = \left[\frac{N_s(\nu', \xi)}{R_s(\theta)} - \frac{N_c(\nu', \xi)}{R_c(\theta)}\right] \sin(\theta)\cos(\theta). \quad (38)$$

Recalling Eqs. (26) and (27) for $R_s(\theta)$, $R_c(\theta)$, respectively,

$$\varepsilon(\theta, \xi) = \frac{1}{qV}\left[\frac{N_s(\nu', \xi)\cos(\theta)}{F_s(\nu_0)} - \frac{N_c(\nu', \xi)\sin(\theta)}{F_c(\nu_0)}\right]. \quad (39)$$

Expanding the noise term,

$$n_j = q'\cos(\nu'\alpha_j)\cos(\xi) - q'\sin(\nu'\alpha_j)\sin(\xi), \quad (40)$$

it is clear that

$$N_s(\nu', \xi) = -q'F_s(\nu')\sin(\xi), \quad (41)$$

$$N_c(\nu', \xi) = q'F_c(\nu')\cos(\xi). \quad (42)$$

The phase error is therefore

$$\varepsilon(\theta, \xi) = \frac{q'}{qV}\left[\frac{F_s(\nu')}{F_s(\nu_0)}\sin(\xi)\cos(\theta) + \frac{F_c(\nu')}{F_c(\nu_0)}\cos(\xi)\sin(\theta)\right]. \quad (43)$$

Using the integral solutions,

$$\frac{1}{2\pi}\int_{\theta=-\pi}^{\pi}[\sin(m\theta)\cos(\theta)]^2 d\theta = \frac{1}{4} \quad (44)$$

and

$$\frac{1}{2\pi}\int_{\theta=-\pi}^{\pi}[\cos(m\theta)\sin(\theta)]^2 d\theta = \frac{1}{4}, \quad (45)$$

for integer values of $m > 1$, the sensitivity to intensity noise as the standard deviation of $\varepsilon(\theta, \xi)$ becomes

$$\text{sens}(\nu') = \frac{1}{2}\sqrt{\left[\frac{F_s(\nu')}{F_s(\nu_0)}\right]^2 + \left[\frac{F_c(\nu')}{F_c(\nu_0)}\right]^2}. \quad (46)$$

This formula tells us the sensitivity of the PSI algorithm to intensity noise at a frequency ν' when the fundamental signal is at a frequency ν_0, which is not necessarily the same as the design frequency $\nu = 1$. For reference, it is recalled that Eqs. (22) and (23) define the filter functions $F_{s,c}(\nu)$.

Figure 5 illustrates the behavior of four of the algorithms listed in Table 1. For these graphs, the solid-line curves (A) correspond to intensity noise sensitivity when the instrument is perfectly tuned and $\nu_0 = 1$. The dashed-line curves (B) are for a fixed detuning error of −20%, meaning that the phase-shift excursion is 20% smaller than the design frequency and therefore $\nu_0 = 0.8$. The horizontal axis is the noise frequency normalized to ν_0. Thus a noise frequency $\nu_0 = 0.8$ appears as a normalized frequency equal to one.

Figure 5 (upper left) shows that the three-frame algorithm is highly sensitive to the second and third harmonics of the fundamental frequency even when perfectly tuned, which makes this algorithm unsuitable even for low-finesse plano Fizeau cavities. The four-frame algorithm of Fig. 5 (upper right) is insensitive to the second harmonic, assuming perfect tuning. This of course is the strongest harmonic; therefore suppressing this frequency is essential to Fizeau interferometry. The dashed-line curve in this figure shows, however, that the suppression of the harmonic distortion is lost when the instrument does not provide interference signals at the design frequency. The 12-frame algorithm shown in Fig. 5 (lower left) suppresses the third harmonic, which leads to negligible sensitivity to Fizeau fringe distortion when the phase shift is properly adjusted across the full field of view. An additional benefit of the 12-frame algorithm is that the derivative of the sensitivity is zero near the second and third harmonics. Nonetheless, at −20% detuning, the sensitivity to the second harmonic is only marginally better than that of the four-frame algorithm. The 15-frame algorithm abandons the suppression of the third harmonic in favor of a broader region about the second-order harmonic, which provides greater detuning resilience for Fizeau cavities of low reflectivity.

7. Multiple Reflections with Phase Shift Detuning

Fizeau fringes contain intensity noise sources at harmonics $\nu = \eta\nu_0$ of integer order $\eta = 2, 3, 4\ldots$ corresponding to the number of round-trip reflections in the Fizeau cavity, where it is recalled that ν_0 is the interference signal frequency, which is usually equal to 1 but allowed to be a variable here to accommodate the detuning error. From Eq. (43), the contributions to the phase-dependent error of each of these multiple reflections is

$$\varepsilon_\eta(\nu_0, \theta) = \frac{q'}{qV}\left[\frac{F_s(\eta\nu_0)}{F_s(\nu_0)}\sin(\eta\theta)\cos(\theta) + \frac{F_c(\eta\nu_0)}{F_c(\nu_0)}\cos(\eta\theta)\sin(\theta)\right], \quad (47)$$

where for a dielectric cavity the synchronous phase value for the additive intensity noise for each reflection η is $\xi = \eta\theta$.

The total phase-dependent error is the sum

$$\varepsilon_{\text{fiz}}(\nu_0, \theta) = \sum_{\eta=2,3,4\ldots}^{\infty}\varepsilon_\eta(\nu_0, \theta). \quad (48)$$

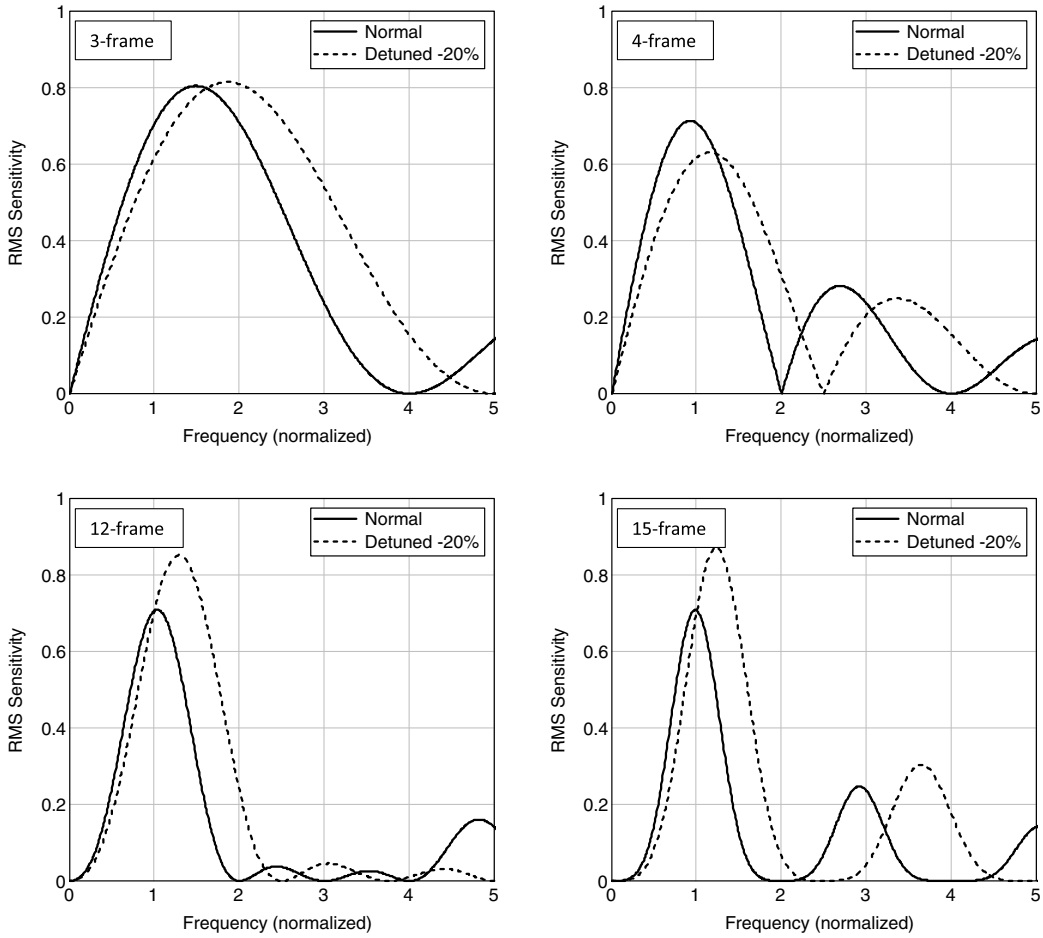

Fig. 5. Sensitivity of PSI algorithms to synchronous intensity noise as a function of frequency for four of the algorithms listed in Table 1. The graphs show results for perfectly adjusted phase shifts (solid line) and a detuning of –20% (dashed line). The second, third, and fourth harmonics present in a Fizeau interferometer signal are at frequencies at 2, 3, and 4, respectively. The frequency scale is normalized to the signal frequency ν_0, which for the solid lines is equal to 1 and for the dashed lines is equal to 0.8. The second-order harmonic is of particular importance because of its strength.

Figure 6 illustrates the calculated total error ε_{fiz} as a function of phase θ for the three-frame algorithm in Table 1. Following Eq. (46) for the RMS intensity sensitivity and assuming that the variances for the various orders η add up independently, the standard deviation of the total error is

$$\sigma_{\text{fiz}}(\nu_0) = \sum_{\eta=2,3,4\ldots}^{\infty} \frac{V_\eta}{2V_1} \sqrt{\left[\frac{F_s(\eta\nu_0)}{F_s(\nu_0)}\right]^2 + \left[\frac{F_c(\eta\nu_0)}{F_c(\nu_0)}\right]^2}. \tag{49}$$

This equation provides the standard deviation of the expected measurement error in a laser Fizeau interferometer as a function of the detuning of the phase shift frequency ν_0, resulting from multiple reflections with the cavity.

The θ-phase dependence for detuning and Fizeau errors is sufficiently different to allow the standard deviations of the errors to be approximated by the root-sum-square method. Thus the net error is

$$\sigma(\nu_0) \approx \sqrt{\sigma_{\text{fiz}}^2(\nu_0) + \sigma_{\text{cal}}^2(\nu_0)}, \tag{50}$$

where $\sigma_{\text{fiz}}(\nu_0)$, $\sigma_{\text{cal}}(\nu_0)$ are from Eqs. (33) and (49). Comprehensive numerical simulation for all the

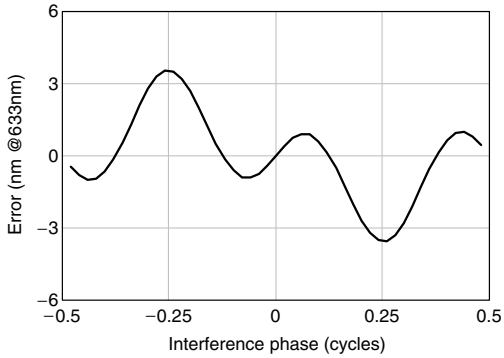

Fig. 6. Phase-dependent measurement errors for the three-frame algorithm in the presence of –20% detuning in a 4%–4% Fizeau cavity.

algorithms verifies this formula up to at least the third Fizeau harmonic.

Figure 7 provides example results of the calculation of Eq. (50) for the four PSI algorithms features in Fig. 5. As expected, the three-frame algorithm is already in trouble with a 4%–4% Fizeau cavity, even for perfect tuning. The four-frame algorithm results in Fig. 7 (upper right) are significantly better, but the benefit disappears with only a few percent detuning. The 12-frame algorithm results in Fig. 7 (lower left) show much better results overall, particularly if the detuning errors stay on the positive side. The 15-frame provides the best overall results for this selection of algorithms, accommodating a range of nearly ±20%. But even for this algorithm, the results can be considered disappointing compared with those of the two-beam calculation, which shows essentially zero error for the entire ±40% display range.

8. Solution Strategies

This paper shows that the effects of phase shift calibration in a spherical Fizeau cavity of modest (4%) reflectivity are dominated by the sensitivity of the data processing to the second-order harmonic distortion in the Fizeau signal. The sensitivity is far greater than usually expected based on error analysis of two-beam interference and, in most cases, overwhelms the benefits of PSI algorithms that have been designed specifically to be highly resistant to detuning.

For general-purpose applications with moderate NA spherical cavities and low reflectivity, the discrepancy between the expected sensitivity and actual performance, although large in a relative sense, is actually quite difficult to detect. The residual error values are small, usually less than 1 nm. These cyclic errors are often less significant than other sources of error, such as cavity misalignment, defocus, vibration, air turbulence, and calibration of the form of the reference surface. This may explain why the detuning error in Fizeau interferometers shows up only rarely in applications requiring high precision, high reflectivity, high NA, or a combination of all three factors [5].

For those configurations where the detuning error is an important source of uncertainty, several solutions are available. For high reflectivity objects, a common remedy is a partially absorptive reference surface coating, which suppresses multiple reflections [26–28]. An additional precaution is to average several data sets with small phase shifts between them, which averages cyclic errors of all types.

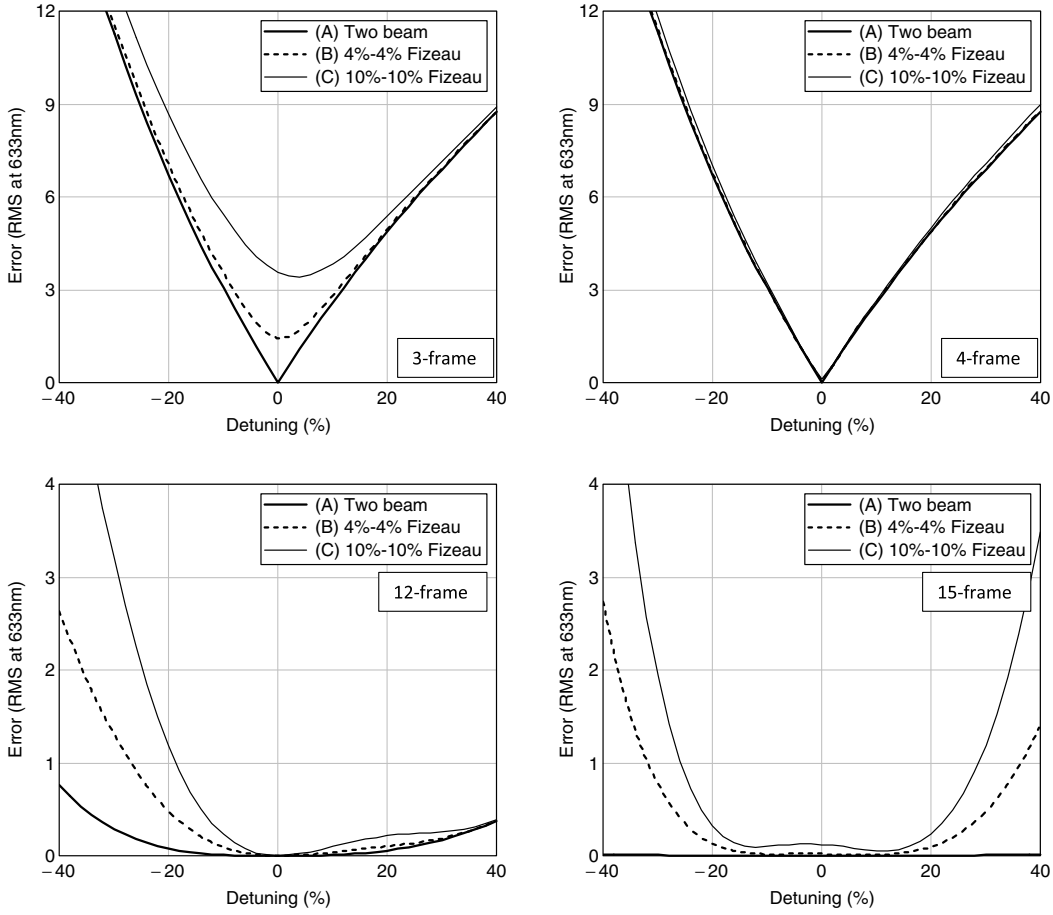

Fig. 7. Sensitivity of PSI algorithms to calibration errors for three different interferometer configurations: (A) Two-beam interferometer. (B) Fizeau interferometer with 4% reflectivity for both surfaces. (C) Fizeau interferometer with 10% reflectivity for both surfaces. Note the 3× change in scale between the upper two graphs and the lower two graphs in the figure.

There is temptation to develop further PSI algorithms, taking into account the importance of the second-order signal harmonic [29]; however, any new algorithm would also need to be robust to nonlinearity, vibration, and random and multiplicative noise. A superior software solution is to set aside the traditional PSI analysis altogether: PSI algorithms based on a single, fixed design frequency are becoming less important as computing power and more advanced processing become available. New adaptive [30] and iterative least-squares methods accommodate not only detuning issues, but many other sources of error that are more prevalent and difficult to control, including in particular environmental vibration [31–33]. Modern commercial interferometers have sufficient horsepower in their data processing to optimize phase estimation without restriction to the interference signal frequency [34]. This appears to be a preferred and more comprehensive solution compared with further development of fixed-frequency PSI algorithms of the traditional form.

In the most demanding applications, the best solution, first recommended by Sommargren in 1986, is to use wavelength tuning in place of mechanical phase shifting, thereby eliminating the field dependence of the phase shift [35]. With advances in enabling technology, modern wavelength-tuned interferometers go well beyond this single advantage, performing a complete Fourier transform of the PSI signal, thereby allowing for rejection of harmonics and other spurious intensity signals [36,37]. Such instruments are ideal for testing spherical cavities, special applications such as homogeneity testing, and for measuring large optics without the need for a mechanical phase shifter [38].

References

1. D. Malacara, M. Servín, and Z. Malacara, "Phase-detection algorithms," in *Interferogram Analysis for Optical Testing*, 2nd ed. (CRC Press, Taylor & Francis Group, 2005), Chap. 6.
2. K. Creath and P. Hariharan, "Phase-shifting errors in interferometric tests with high-numerical-aperture reference surfaces," Appl. Opt. **33**, 24–25 (1994).
3. P. de Groot, "Phase-shift calibration errors in interferometers with spherical Fizeau cavities," Appl. Opt. **34**, 2856–2863 (1995).
4. K. Hibino, B. F. Oreb, D. I. Farrant, and K. G. Larkin, "Phase shifting for nonsinusoidal waveforms with phase-shift errors," J. Opt. Soc. Am. A **12**, 761–768 (1995).
5. K. Creath, "Choosing a phase-measurement algorithm for measurement of coated LIGO optics," Proc. SPIE **4101**, 46 (2000).
6. B. Zhao and Y. Surrel, "Phase shifting: six-sample self-calibrating algorithm insensitive to the second harmonic in the fringe signal," Opt. Eng. **34**, 2821–2822 (1995).
7. P. J. de Groot, "Long-wavelength laser diode interferometer for surface flatness measurement," Proc. SPIE **2248**, 136–140 (1994).
8. N. A. Massie and S. Holly, "Quasi-real time high precision characterization of active mirrors," Proc. SPIE **0141**, 82–87 (1978).
9. J. H. Bruning, D. R. Herriott, J. E. Gallagher, D. P. Rosenfeld, A. D. White, and D. J. Brangaccio, "Digital wavefront measuring interferometer for testing optical surfaces and lenses," Appl. Opt. **13**, 2693–2703 (1974).
10. R. C. Moore and F. H. Slaymaker, "Direct measurement of phase in a spherical-wave Fizeau interferometer," Appl. Opt. **19**, 2196–2200 (1980).
11. P. Hariharan, "Digital phase-stepping interferometry: effects of multiply reflected beams," Appl. Opt. **26**, 2506–2507 (1987).
12. G. Bönsch and H. Bohme, "Phase determination of Fizeau interferences by phase shifting interferometry," Optik **82**, 161–164 (1989).
13. B. V. Dorrío, J. Blanco-García, C. López, A. F. Doval, R. Soto, J. L. Fernández, and M. Pérez-Amor, "Phase error calculation in a Fizeau interferometer by Fourier expansion of the intensity profile," Appl. Opt. **35**, 61–64 (1996).
14. P. de Groot, "Phase shifting interferometer and method for surface topography measurement," U.S. patent 5,473,434 (December 5, 1975).
15. Y. Surrel, "Additive noise effect in digital phase detection," Appl. Opt. **36**, 271–276 (1997).
16. K. Hibino, "Error-compensating phase measuring algorithms in a Fizeau interferometer," Opt. Rev. **6**, 529–538 (1999).
17. Y. Surrel, "Design of algorithms for phase measurements by the use of phase stepping," Appl. Opt. **35**, 51–60 (1996).
18. D. Malacara, M. Servín, and Z. Malacara, "Periodic signal phase detection and algorithm analysis," in *Interferogram Analysis for Optical Testing*, 2nd ed. (CRC Press, Taylor & Francis Group, 2005) Chap. 5.
19. H. Schreiber and J. H. Bruning, "Phase shifting interferometry," in *Optical Shop Testing*, D. Malacara, ed. (Wiley, 2006), pp. 547–666.
20. J. Wesner, J. Heil, and H.-M. Heuck, "High NA absolute Fizeau phase shifting interferometry," in *DGaO Proceedings* (2009), paper C16.
21. K. Freischlad and C. L. Koliopoulos, "Fourier description of digital phase-measuring interferometry," J. Opt. Soc. Am. A **7**, 542–551 (1990).
22. J. C. Wyant, C. L. Koliopoulos, B. Bhushan, and O. E. George, "An optical profilometer for surface characterization of magnetic media," Trans. ASLE **27**, 101–113 (1984).
23. J. C. Wyant, "Use of an ac heterodyne lateral shear interferometer with real-time wavefront correction systems," Appl. Opt. **14**, 2622–2626 (1975).
24. P. de Groot, "Derivation of algorithms for phase-shifting interferometry using the concept of a data-sampling window," Appl. Opt. **34**, 4723–4730 (1995).
25. P. J. de Groot, "Vibration in phase-shifting interferometry," J. Opt. Soc. Am. A **12**, 354–365 (1995).
26. P. B. Clapham and G. D. Dew, "Surface-coated reference flats for testing fully aluminized surfaces by means of the Fizeau interferometer," J. Sci. Instrum. **44**, 899–902 (1967).
27. J. F. Biegen, "Coating and method for testing plano and spherical wavefront producing optical surfaces and systems having a broad range of reflectivities," U.S. patent 4,820,049 (April 11, 1989).
28. Zygo Corporation, "Transmission spheres," Product Specifications SS-0043 (2014).
29. K. Hibino, B. F. Oreb, D. I. Farrant, and K. G. Larkin, "Phase-shifting algorithms for nonlinear and spatially nonuniform phase shifts," J. Opt. Soc. Am. A **14**, 918–930 (1997).
30. P. de Groot, "Apparatus and method for mechanical phase shifting interferometry," U.S. patent 7,030,995 (April 18, 2006).
31. L. L. Deck, "Phase-shifting interferometry in the presence of vibration," U.S. patent 7,796,273 (September 14, 2010).
32. L. L. Deck, "Phase-shifting interferometry in the presence of vibration using phase bias," U.S. patent 7,796,275 (September 14, 2010).
33. J. Xu, Q. Xu, L. Chai, and H. Peng, "Algorithm for multiple-beam Fizeau interferograms with arbitrary phase shifts," Opt. Express **16**, 18922–18932 (2008).
34. Zygo Corporation, "Verifire QPZ Interferometer System," Product Specifications SS-0091 (2012).
35. G. E. Sommargren, "Interferometric wavefront measurement," U.S. patent 4,594,003 (June 10, 1986)
36. P. de Groot, "Measurement of transparent plates with wavelength-tuned phase-shifting interferometry," Appl. Opt. **39**, 2658–2663 (2000).
37. L. L. Deck, "Fourier-transform phase-shifting interferometry," Appl. Opt. **42**, 2354–2365 (2003).
38. Zygo Corporation, "Verifire MST Interferometer System for Multiple Surface Testing," Product Specifications SS-0034 (2012).